11-18-2013

Design Considerations Regarding Ellipsoidal Mirror Based Reflectometers

Michael R. Benson

Michael A. Marciniak
Air Force Institute of Technology

Recommended Citation

Michael R. Benson and Michael A. Marciniak, "Design considerations regarding ellipsoidal mirror based reflectometers," Opt. Express 21, 27519-27536 (2013). https://doi.org/10.1364/OE.21.027519

Design considerations regarding ellipsoidal mirror based reflectometers

Michael R. Benson* and Michael A. Marciniak
Department of Engineering Physics, Air Force Institute of Technology, Wright-Patterson AFB Ohio 45433, USA
**michael.benson@afit.edu*

Abstract: Hemi-ellipsoidal mirrors are used in reflection-based measurements due to their ability to collect light scattered from one focal point at the other. In this paper, a radiometric model of this energy transfer is derived for arbitrary mirror and detector geometries. This model is used to examine the imaging characteristics of the mirror away from focus for both diffuse and specular light. The radiometric model is applied to several detector geometries for measuring the Directional Hemispherical Reflectance for both diffuse and specular samples. The angular absorption characteristics of the detector are then applied to the measurement to address measurement accuracy for diffuse and specular samples. Examining different detector configurations shows the effectiveness of flat detectors at angles ranging from normal to 50°, and that multifaceted detectors can function from normal incidence to grazing angles.

OCIS codes: (120.5820) Scattering measurements; (120.4570) Optical design of instruments; (120.5700) Reflection; (120.1840) Densitometers, reflectometers.

References and links

1. W. M. Brandenberg, "Focusing properties of hemispherical and ellipsoidal mirror reflectometers," J. Opt. Soc. Am. **54**, 1235–1237 (1964).
2. J. Workman Jr and A. Springsteen, *Applied Spectroscopy: A Compact Reference for Practitioners* (Access Online via Elsevier, 1998).
3. J. Lorincik and J. Fine, "Focusing properties of hemispherical mirrors for total integrating scatter instruments," Appl. Optics **36**, 8270–8274 (1997).
4. R. P. Heinisch and E. M. Sparrow, "Efficiency characteristics of hemi-ellipsoidal and hemispherical collectors of thermal radiation," Int. J. Heat Mass Transfer **14**, 1275–1284 (1970).
5. R. P. Heinisch, F. J. Bradac, and D. B. Perlick, "On the fabrication and evaluation of an integrating hemiellipsoid," Appl. Optics **9**, 483–487 (1970).
6. E. Hecht, *Optics* (Addison-Wesley, 2002).
7. R. W. Boyd, *Radiometry and the Detection of Optical Radiation* (John Wiley and Sons, 1983).
8. K. A. Snail and L. M. Hanssen, "Magnification of conic mirror reflectometers," Appl. optics **37**, 4143–4149 (1998).
9. K. A. Snail, "Reflectometer design using nonimaging optics," Appl. Optics **26**, 5326–5332 (1987).
10. B. E. Wood, J. G. Pipes, A. M. Smith, and J. A. Roux, "Hemi-ellipsoidal mirror infrared reflectometer: development and operation," Appl. Optics **15**, 940–950 (1976).
11. M. R. Benson, M. A. Marciniak, and J. W. Burks, "Characterization and measurements collected from infrared grazing angle reflectometer," in "Proc. SPIE," , vol. 8154 (2011), vol. 8154, p. 81541B.
12. M. R. Benson, M. A. Marciniak, and J. W. Burks, "Measuring grazing-angle dhr with the infrared grazing angle reflectometer," in "Proc. SPIE," (International Society for Optics and Photonics, 2012), pp. 84950R–84950R.
13. W. R. Blevin and W. J. Brown, "An infra-red reflectometer with a spheroidal mirror," J. Sci. Instrum. **42**, 385–389 (1965).

#190358 - $15.00 USD Received 16 May 2013; revised 19 Aug 2013; accepted 22 Aug 2013; published 4 Nov 2013

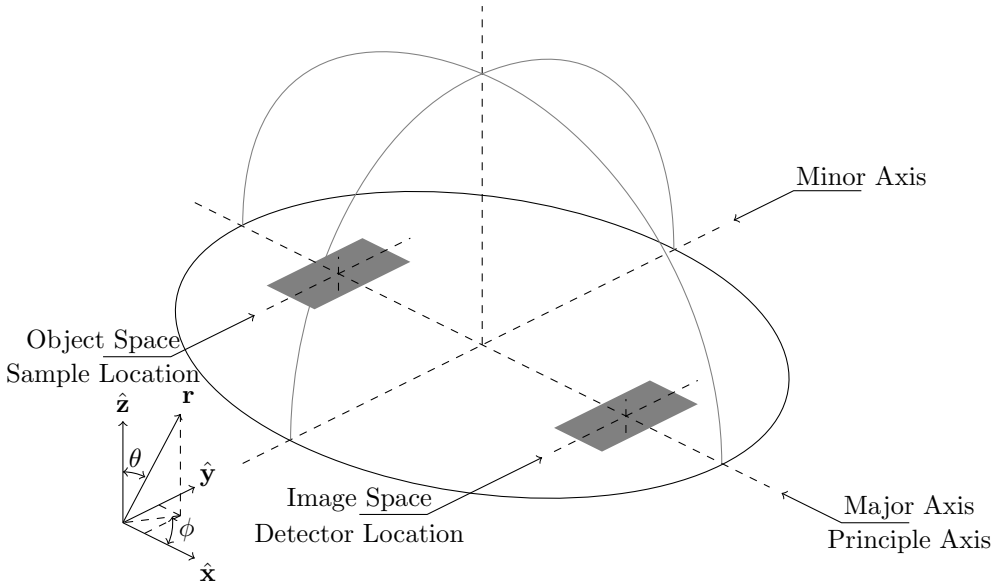

Fig. 1. Diagram of a hemi-ellipsoidal mirror used for making reflectance measurements. The sample is placed at the upper focus, in object space, while the detector is located at the lower focus, in image space.

1. Introduction

Directional Hemispherical Reflectance (DHR) is a metric used to describe the ratio of light reflected from a surface to the light incident at a given angle of incidence. Because this metric requires measuring the total amount of light reflected, the measurement instrument must be able to capture all light reflected over the front hemisphere of the sample. One design for doing this is using a hemi-ellipsoidal mirror to collect all of the scattered light. The sample is located at one focus of the mirror, while a detector is located at the opposite focus, as shown in Fig. 1. All of the light scattered by the sample is reflected by the mirror to the second focal point, where the detector measures the total light reflected from the sample.

2. Image formation

Several authors have defined closed-form relationships between object space and image space for spherical and hemi-ellipsoidal mirrors. Brandenburg [1] derived a solution which depends on knowing the point in object space and the point of reflection on the mirror. This assumption allows a maximum magnification factor to be derived for the objects which are small and close to the focal point of the mirror. This model accurately models the imaging characteristics of the system, but is not radiometrically accurate. It assumes that the light reflected from the sample is all scattered to a single point on the mirror. In system utilizing laser illumination (a $\theta/2\pi$ system, as defined by [2]), light is specularly reflected from the sample as a cylinder; each reflected ray is parallel to one another. Several other author's use Brandenberg's derivation as the basis of their work [3–5].

This fundamental difference in derivations means that Brandenberg's work cannot be extended to a radiometric model of the system. By treating the light in this fashion, a specular sample, and eventually a diffuse sample, can be properly modeled and analyzed. In addition,

#190358 - $15.00 USD Received 16 May 2013; revised 19 Aug 2013; accepted 22 Aug 2013; published 4 Nov 2013

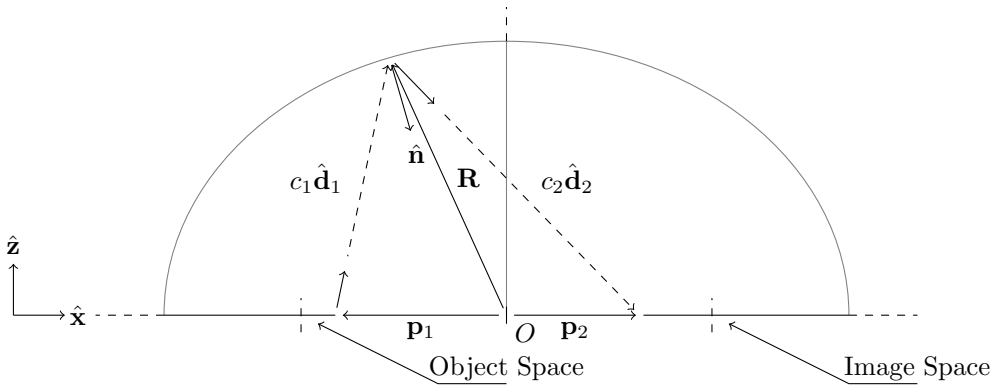

Fig. 2. Given two vectors $\mathbf{p}_1$, which is the object point, and $\hat{\mathbf{d}}_1$, which is the direction of the ray, there are two values of c_1 which place the vector $\mathbf{R}$ on the surface of the ellipsoid. $\hat{\mathbf{d}}_2$ is found by reflecting $\hat{\mathbf{d}}_1$ across the normal at $\mathbf{R}$. In this case, c_2 is found by solving for where $\mathbf{p}_2$ has a zero $\hat{\mathbf{z}}$ component.

this allows two of Snail's and Hanssen's sources of error to be easily addressed [2]. The following derivation directly addresses magnification error, and is easily extended in Section 5 to address the detector's angular response.

The focal point of the mirror is the only point which can form a perfect image of a point in object space [6]. Off focus, the system forms an aberrated spot. While this prevents perfect imaging, it can still be used to measure energy transfer from object space to image space. Although a single image point does not exist for most points in object space for ellipsoidal mirrors, geometrical optics can be used to calculate energy transfer. Rays will be launched from object space and reflected off the mirror into image space to analyze the ability of a detector to capture light scattered from the sample.

Figure 2 presents the geometry involved in this problem. Given a ray passing through the point $\mathbf{p}_1$ traveling at an angle $\hat{\mathbf{d}}_1$, the point at which this ray intersects the mirror can be expressed as $\mathbf{R} = \mathbf{p}_1 + c_1\hat{\mathbf{d}}_1$. Because $\mathbf{R}$ is some point on the ellipsoidal mirror, the ellipsoid equation can be used to calculate c_1, which is some constant which makes the following equation true:

$$\frac{\left[\left(\mathbf{p}_1 + c_1\hat{\mathbf{d}}_1\right)\cdot\hat{\mathbf{x}}\right]^2}{r_{\text{major}}^2} + \frac{\left[\left(\mathbf{p}_1 + c_1\hat{\mathbf{d}}_1\right)\cdot\hat{\mathbf{y}}\right]^2}{r_{\text{minor}}^2} + \frac{\left[\left(\mathbf{p}_1 + c_1\hat{\mathbf{d}}_1\right)\cdot\hat{\mathbf{z}}\right]^2}{r_{\text{minor}}^2} = 1. \tag{1}$$

where r is the associated radius of the mirror, and $\hat{\mathbf{x}}, \hat{\mathbf{y}}$ and $\hat{\mathbf{z}}$ are the components of the rectangular coordinates as shown in Fig. 1 and Fig. 2. Knowing where this ray intersects the mirror, the normal to this point can easily be calculated, and the new direction of propagation calculated using vector reflection.

Again, the goal is to identify where this reflected ray intersects the plane of the detector. For the case of a flat detector, the detector is mounted on the axis of the mirror, where $z = 0$, as in Fig. 1. Defining $\mathbf{p}_2$ in the same way as $\mathbf{p}_1$, the point of intersection is

$$\mathbf{p}_2 = \mathbf{p}_1 + c_1\hat{\mathbf{d}}_1 - \frac{\mathbf{p}_1\cdot\hat{\mathbf{z}} + c_1(\hat{\mathbf{d}}_1\cdot\hat{\mathbf{z}})}{2(\hat{\mathbf{d}}_1\cdot\hat{\mathbf{n}})(\hat{\mathbf{n}}\cdot\hat{\mathbf{z}}) - \hat{\mathbf{d}}_1\cdot\hat{\mathbf{z}}}\left[2(\hat{\mathbf{d}}_1\cdot\hat{\mathbf{n}})\hat{\mathbf{n}} - \hat{\mathbf{d}}_1\right] \tag{2}$$

where $\hat{\mathbf{n}}$ is the unit normal vector at the point $\mathbf{R}$. It is important to note that this equation is strictly a function of $\mathbf{p}_1$ and $\hat{\mathbf{d}}_1$.

#190358 - $15.00 USD Received 16 May 2013; revised 19 Aug 2013; accepted 22 Aug 2013; published 4 Nov 2013

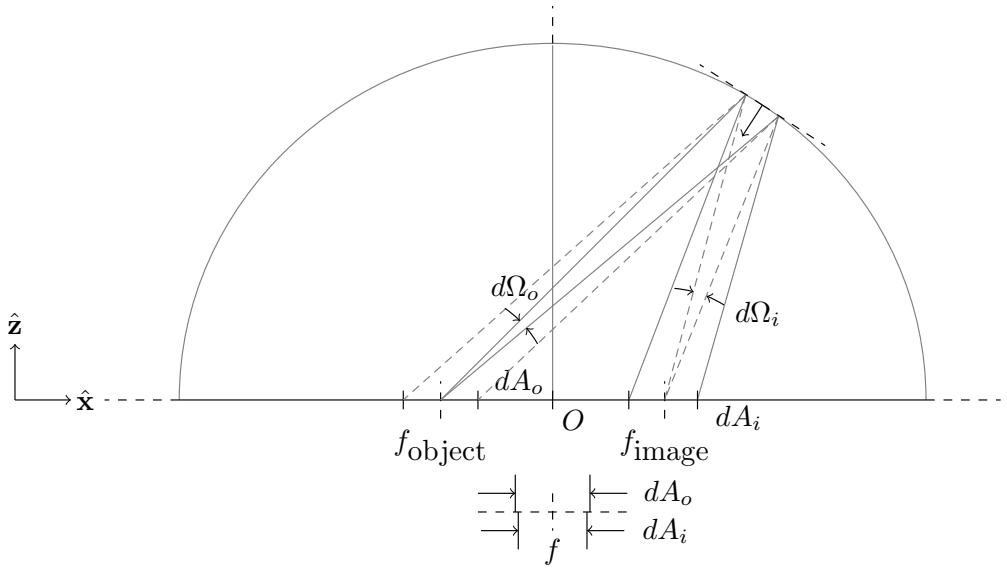

Fig. 3. The radiance theorem shows that the radiance emitted in object space will be equal to that reflected by the mirror into image space. Because the mirror deforms the differential area, it is easier to perform calculations in object space. Imaging is used to calculate the new location of the differential area. If this differential area is within the geometry of the detector, this portion of the radiance emitted in object space is detected.

A radiometric model for the flux emitted from a sample can be given as

$$\Phi = \int_{A_o} \int_{\Omega_o} L(\hat{\mathbf{d}}_i; \mathbf{p}_1, \hat{\mathbf{d}}_1)(\mathbf{d}_1 \cdot \hat{\mathbf{z}})\, d\Omega_o\, dA_o, \tag{3}$$

where dA_o is the differential area of the sample, $d\Omega_o$ is the differential solid angle into which the flux is emitted, and L is the radiance emitted from the point $\mathbf{p}_1$. It is important to note that $d\Omega_o$ is defined in object space. The radiance can be separated into angular information and positional information by defining it as

$$L(\hat{\mathbf{d}}_i; \mathbf{p}_1, \hat{\mathbf{d}}_1) = E_0(\mathbf{p}_1) f(\hat{\mathbf{d}}_i; \hat{\mathbf{d}}_1) \tag{4}$$

where E_0 is the incident irradiance, and f is the Bidirectional Reflectance Distribution Function (BRDF) of the sample. Throughout the rest of this paper, all BRDFs will be either perfectly specular or perfectly diffuse. It is important to note that no sample is perfectly specular or perfectly diffuse. These two cases are presented to demonstrate the issues present in the limiting cases of the measurement.

The radiance theorem shows that radiance is preserved through reflectance [7]. This means that the differential solid angle multiplied by the differential area will be the same in object space and image space. Because the solid angle changes upon reflection, the differential area in image space must be different than the differential area in object space. This effect is shown in Fig. 3. Notice that the differential area dA_i is smaller than dA_o. The difference between the two is related to both the position of the differential area and the angle of the differential solid angle.

This inconsistency makes integration in image space very difficult. However, using the geometry discussed earlier, the location of the differential area can be easily located. If the differential

#190358 - $15.00 USD Received 16 May 2013; revised 19 Aug 2013; accepted 22 Aug 2013; published 4 Nov 2013

area in image space is within the geometry of the detector, the total power scattered into the associated solid angle is properly measured by the detector. Mathematically, this is performed as a detection function, D, which is a function of both position and angle in object space. This allows the radiometric calculations to be carried out in object space instead of image space.

Rewriting Eq. (3) to include this detection term and the expanded radiance of Eq. (4), the power detected is

$$\begin{aligned}\Phi_d &= \int_{A_o}\int_{\Omega_o} E_o(\mathbf{p}_1) f(\hat{\mathbf{d}}_i;\hat{\mathbf{d}_1})(\hat{\mathbf{d}}_1\cdot\hat{\mathbf{z}}) D\left[\mathbf{p}_2(\mathbf{p}_1,\hat{\mathbf{d}}_1)\right] d\Omega_o\, dA_o \\ &= \int_{A_o} E_o(\mathbf{p}_1) E_d(\hat{\mathbf{d}}_i,\mathbf{p}_1) dA_o \end{aligned} \tag{5}$$

where

$$E_d(\hat{\mathbf{d}}_i,\mathbf{p}_1) \equiv \int_{\Omega_o} f(\hat{\mathbf{d}}_i;\hat{\mathbf{d}_1})(\hat{\mathbf{d}}_1\cdot\hat{\mathbf{z}}) D\left[\mathbf{p}_2(\mathbf{p}_1,\hat{\mathbf{d}}_1)\right] d\Omega_o. \tag{6}$$

Due to the detector function's dependence on $\mathbf{p}_2$, which is a function of both angle and position, the integral cannot be simplified. The angular integration can be carried out first, which allows E_d, defined here as the unitless detectable irradiance map in object space, to be calculated first. The detectable irradiance can then be multiplied by the area of the sample, and integrated over object space. Holding the size and shape of the sample constant while allowing the position to change over the range of positions is mathematically the same as performing a 2D convolution between the incident irradiance and the detected irradiance map. This allows a wide range of sample sizes, shapes and positions to be readily analyzed for a single detector configuration.

3. Image distortion

Before using Eq. (5) to examine detector performance, the power transfer between object space and image space must be examined. The simplest cases to examine are the cases of light scattered from either perfectly diffuse or perfectly specular surfaces. For specular samples, the power is always imaged point to point. Here, the image distortions caused by the mirror will be examined. A diffuse scatter distributes power over an area, so the energy distribution will be examined.

The image of a point source is the point where all rays leaving the object intersect each other in image space. In the case of a hemi-ellipsoidal mirror, this only occurs perfectly between the two foci. The mirror fails to properly image all other points. Because of this, the intersection of the rays with plane of the object will be used to define the image point, which is what was derived in Section 2.

Note that the geometry of the mirror plays an important role in image formation and power transfer. All of the simulations carried out here use a mirror with a major radius of 10 units, and a minor radius of 9.8 units. This gives an eccentricity of $\varepsilon \equiv f/r_{\text{major}} = 0.2$ for the mirror examined here. These dimensions were chosen because they demonstrate the deformations caused by the hemi-ellipsoidal mirror, and were studied previously [1].

Figure 4 shows the setup for an experiment in which five point sources with Lambertian scatter patterns are imaged by the mirror. Light is emitted to the entire 2π steradian hemisphere towards the mirror, and is then reflected into image space. The irradiance in image space is shown in Fig. 5. The center scatterer (c) images perfectly at the opposite focal point, which is entirely consistent with the definition of an ellipsoid. Off focus, the light is distributed over a large area. The point (b) is between the focal point and the center of the mirror along the principle axis, and is imaged to an aberrated area which is spread out along this same axis. The fact that the light is concentrated along this axis is due to the rotational symmetry of the

#190358 - $15.00 USD Received 16 May 2013; revised 19 Aug 2013; accepted 22 Aug 2013; published 4 Nov 2013

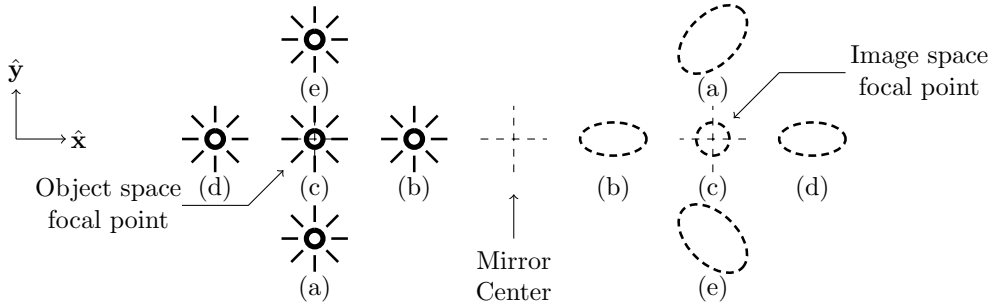

Fig. 4. Schematic of five points with Lambertian radiance located near the object space focal point which are imaged into image space.

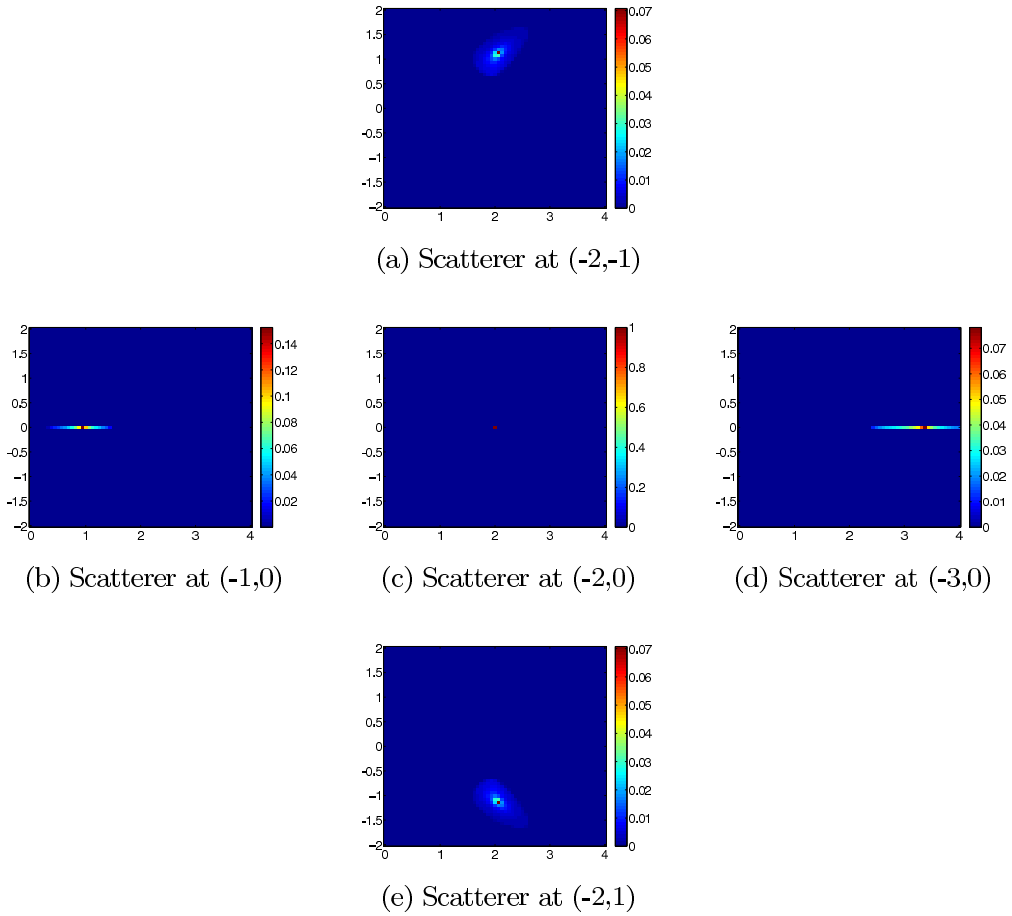

(a) Scatterer at (-2,-1)

(b) Scatterer at (-1,0)

(c) Scatterer at (-2,0)

(d) Scatterer at (-3,0)

(e) Scatterer at (-2,1)

Fig. 5. The irradiance of five point sources in object space (as shown in Fig. 4) are imaged into image space. The middle point (c) is the point located at the focus, and is best imaged. Note that both points located off focus on the principle axis, (b) and (d), are blurred only along that axis. The points located perpendicular to this axis, (a) and (e), are blurred significantly more, and are symmetrical about the principle axis.

#190358 - $15.00 USD Received 16 May 2013; revised 19 Aug 2013; accepted 22 Aug 2013; published 4 Nov 2013

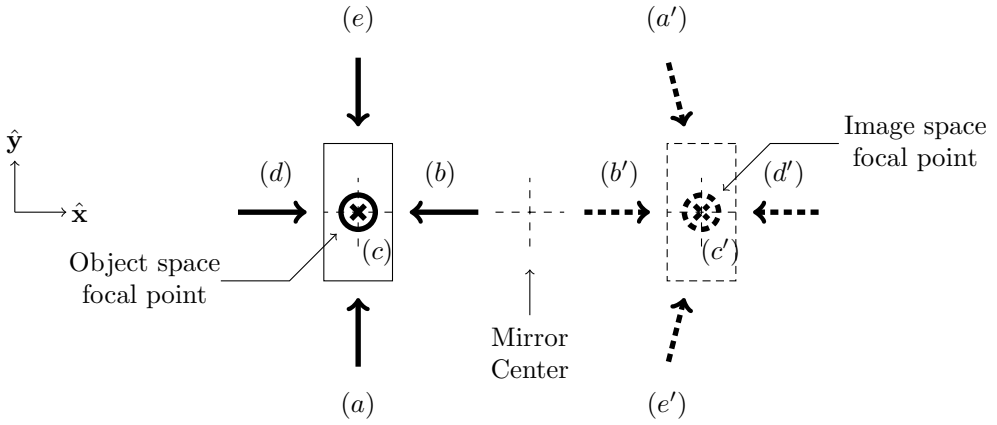

Fig. 6. Schematic of a rectangularly shaped object uniformly illuminated in object space using light that is incident along the vectors (*a*)-(*e*). These rays are reflected off the object towards the mirror, which reflects them into image space along the dashed vectors (a')-(e'). The image point is defined as the point where these rays intersect the plane of the object in image space. Note that vectors (*a*),(*b*),(*d*) and (*e*) are oriented at $\theta = 45^\circ$, while (*c*) is oriented at normal.

hemi-ellipsoid. The point (d), which is located along the same axis on the opposite side of the focus, is spread out along the same axis.

The points off of the principle axis have much more complex irradiance distributions. The highest irradiance is scattered close to the location of the paraxial image point. Only about 20% of the scattered power is located around the paraxial image location, the rest is spread out over an area of 0.8 units-squared. This energy distribution is something that needs to be addressed during system design. The scattered irradiance from points (a) and (e) are symmetric about the principle axis.

Figure 6 sets up a simulation where an object is imaged using specular light oriented at different angles. In the diffuse case, a single point will create an aberrated area in image space, so a single point is imaged. For the specular case, a single point will always be imaged to a single point in object space. Again, the image point is defined as the point where the reflected ray intersects the plane of the object. The image of the object illuminated with the rays detailed in Fig. 6 is shown in Fig. 7.

The plot (c') of Fig. 7 shows the image that is formed of an object illuminated using light that is incident parallel to the object's normal axis. The image formed is significantly distorted, especially at the points that are farthest away from the focal point of the mirror. It is very important to note that the image formed is bigger than the object. The plot (d') shows the image formed when the reflected light strikes the front of the mirror, the portion farthest away from object-space focal point. This has a collecting effect on the image; the image is smaller here than it is in (c'). (b') shows light reflected off the opposite end of the mirror, which has the opposite effect: (b') makes an image which is substantially larger than (d'). At an 85° angle of incidence, (d') has an area of 7.66 units-squared (96% of object), which is substantially smaller than the area of (c'), which is 12.58 units-squared (160% of object).

(a') and (e') are images made using light that is parallel to the narrow portion of the object. The most important feature to note is the way that the mirror distorts the corners of the object. This is a function of angle of incidence. Higher angles result in more severe distortion. These

#190358 - $15.00 USD Received 16 May 2013; revised 19 Aug 2013; accepted 22 Aug 2013; published 4 Nov 2013

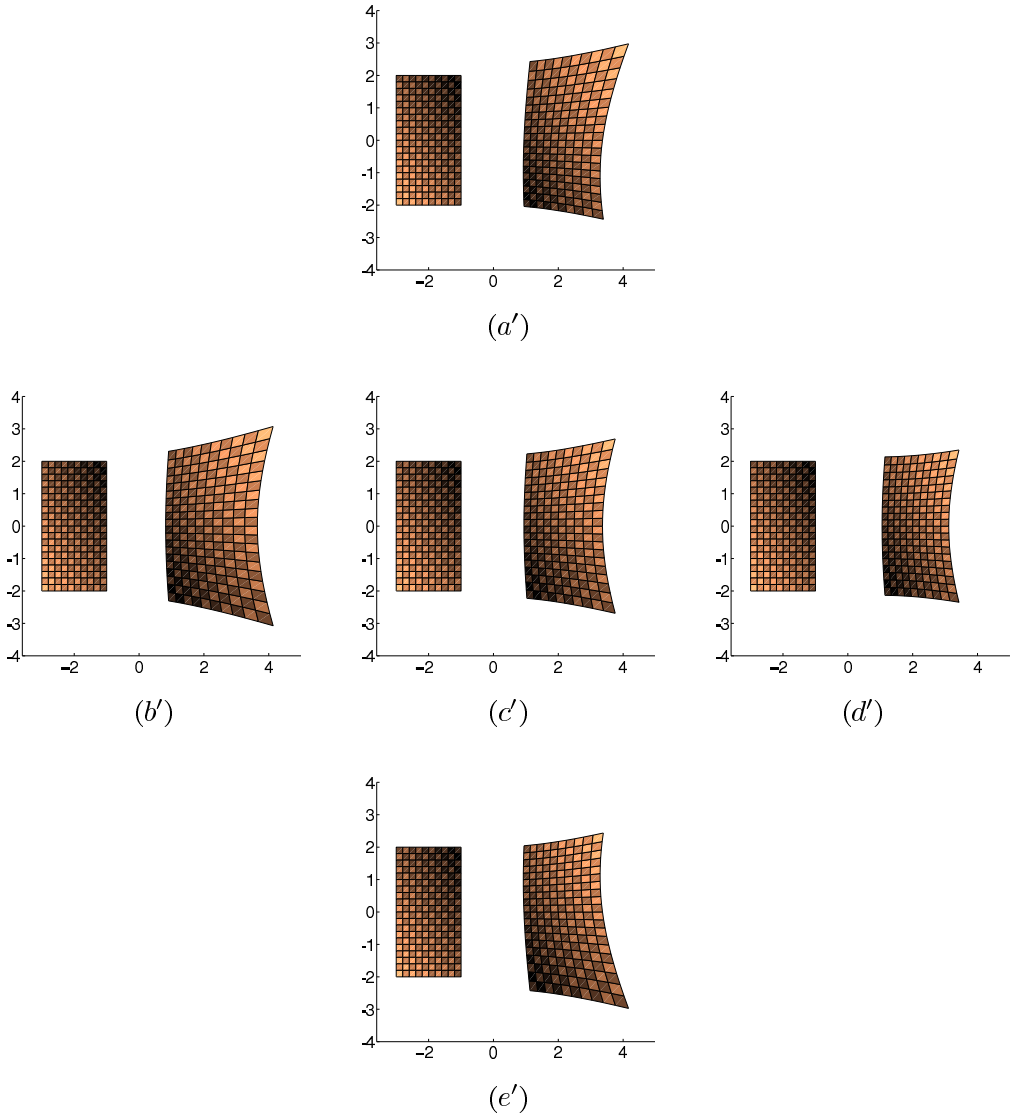

Fig. 7. A perfectly specular sample (shown on the left of each plot) is imaged using light incident parallel to the rays detailed in Fig. 6. Note that (a') is the reflection of (a) off the sample, then the mirror.

#190358 - $15.00 USD Received 16 May 2013; revised 19 Aug 2013; accepted 22 Aug 2013; published 4 Nov 2013

distortions change the shape of the image in image space, but do not significantly change the area. At 85° angle of incidence, the area of the image is around 13.75 units-squared (172% of object). This is not appreciably bigger than the area of the image at normal incidence, which is 12.58 units-squared (157% of object). However, the shape of the image changes significantly. (a') is extended further to the upper right than (c'). At angles close to normal incidence, these distortions do not change significantly. At higher angles, the location and shape of the image varies as a function of angle, an effect which needs to be accounted for during system design.

These ray tracing models are consistent with the work presented by Brandenburg [1] and Snail [8]. Their work presents a maximum magnification as a function of mirror eccentricity. This work shows that the actual image formed by a specular target is within this magnification. The additional analysis here is that the shape formed is smaller than the bounds of the magnification, which means that the detector in the system can be smaller than the bounds. This leads to an overall better system design, which will be discussed in the later sections.

The simulation shown above seems to imply that a design with light striking the sample along the vector (d) shown in Fig. 6 would be the best experimental setup. In this case, at higher angles of incidence, the mirror has a collecting effect on the light scattered by the object, which would allow the detector to be made smaller. In practice, this is not the case. Typically, DHR systems such as this are illuminated with laser light sources. The illuminated area cast by these kinds of sources grows as a function of the angle of incidence, proportional to $1/\cos\theta$. Because of this, the object would have to be rotated 90° from that shown in Fig. 6 and Fig. 7. At normal incidence, the image cast by the system in this configuration is significantly larger than the one detailed above, covering an area of 14.75 units-squared (185% of object). Because of this effect, the remainder of this paper examines system setups where the light is incident along (a). This is the simplest experimental setup that will allow the largest possible sample for a given detector size.

4. Size of the detector

Using Eq. (5), the power collected by the detector can be calculated given the shape and BRDF of the sample, and the shape of the detector. The total power scattered by the sample can also be found using the same equation, assuming that the detection term is omitted. Note that, for now, it is assumed that every ray which hits the detector is properly detected. In practice, this is not necessarily true, motivating Section 5. Other authors have approached this problem by calculating the maximum magnification of the system [1, 8], with the intent of using this metric to calculate the minimum detector size. This research aims for a more rigorous solution by calculating the maximum spot size that can be detected by some detector.

Figures 8, 10 and 12 are the detectable irradiance of the system for an associated BRDF distribution. All of these plots are normalized to the peak detectable irradiance at the given angle. For the majority of the specular cases, there is a clearly defined area in object space for which the associated detector can properly measure the reflected power. This is not the case for a diffuse scatterer. For example, rays which are scattered at high angles of incidence are sometimes scattered too far away from the detector to be properly detected, even though rays scattered at normal incidence are properly detected. The total scattered power can only be measured from a much smaller area in object space. To calculate the power measured by the detector, the detectable irradiance map can be multiplied by the shape of the object and integrated, as seen in Eq. (5).

In a real system, the sample will be typically illuminated using a laser light source, for which the spot size changes as a function of angle of incidence. The length of the illuminated area increases by a factor of $1/\cos\theta_i$. Therefore, the spot size is a much longer ellipse at high angles of incidence, which is something that needs to be accounted for in the model.

#190358 - $15.00 USD Received 16 May 2013; revised 19 Aug 2013; accepted 22 Aug 2013; published 4 Nov 2013

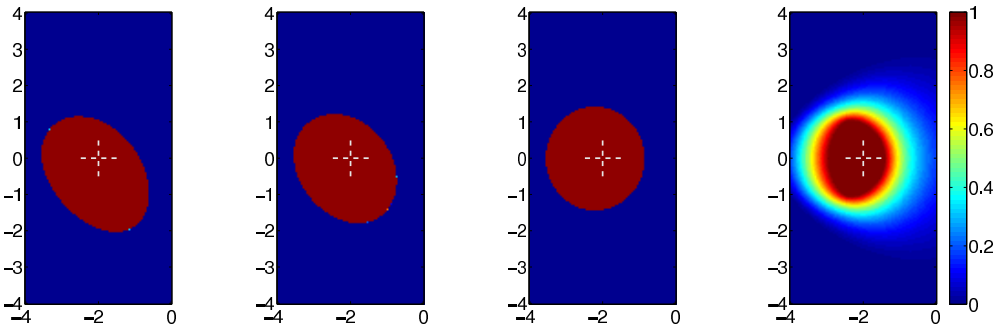

(a) $\theta_i = 85°$ (b) $\theta_i = 45°$ (c) $\theta_i = 0°$ (d) Diffuse Case

Fig. 8. Detectable irradiance map for a circular detector with radius 1.596 units (surface area = 8 units-squared) and a mirror with the dimensions given in Section 3. The white cross is the location of the object-space focal point.

Each detector will be evaluated on three different criteria. The first is maximum spot size for light incident at normal incidence. The second is maximum spot size which works for all angles between normal and 60° from normal. This allows the detector to be used over a wide range of measurements without significantly impacting system design. The last criterion is the maximum spot size which works for all angles between normal and 85° from normal. This allows the instrument to make grazing-angle measurements. These measurements are important for some instruments, but will significantly impact the maximum spot size. Spot sizes will be defined in terms of $\delta \equiv r_s/r_{\text{major}}$, where r_s is the radius of the spot at normal incidence.

Three different detector configurations will be examined. All three detector configurations will share the same surface area, which is 8 units-squared. The first detector configuration is circular. This shape is closest to the image shape formed by light incident at normal incidence, which implies that it will work best with measurements close to normal. The next detector configuration will be an ellipse with a major axis two times longer than the minor axis. This should allow better detection of light at higher angles of incidence than the circular case, but should not perform as well as the circular case at angles closer to normal incidence. The final case will be a rectangular detector with the a width-to-height ratio of 2:1. The three dimensional detector examined in Section 5 is an extension of this configuration.

It is important to note that all of these analyses were performed using the mirror geometry detailed in Section 3; this mirror has a major radius of 10 units and a minor radius of 9.8 units, giving it an eccentricity of $\varepsilon = 0.2$. Making the mirror bigger or smaller with respect to the dimensions of the detector will affect the results of these simulations, and will be examined briefly at the end of this section.

The detectable irradiance map for the circular detector is shown in Fig. 8. This detector can accurately measure samples sizes with $\delta = 0.098$ with less than 1% error. This measurement has a detector-radius-to-sample-radius ratio of $\sim$1.6, which is consistent with the work presented by Heinisch and Sparrow [4]. For the normal-to-60-degree measurement, the maximum δ decreases to 0.068, with the same error. Including grazing angles, the radius of the spot size decreases dramatically to $\delta = 0.0104$, with the same error. Plots of this detector's efficiency as a function of angle are shown in Fig. 9.

The elliptical detector functions best at high angles of incidence. Detectable irradiance maps are shown in Fig. 10. For the case of normal incidence, the detector could accurately measure a sample with $\delta = 0.050$ with less than a 1% error. This is slightly more than half of the sample radius associated with the circular detector at normal incidence. This is not surprising;

#190358 - $15.00 USD Received 16 May 2013; revised 19 Aug 2013; accepted 22 Aug 2013; published 4 Nov 2013

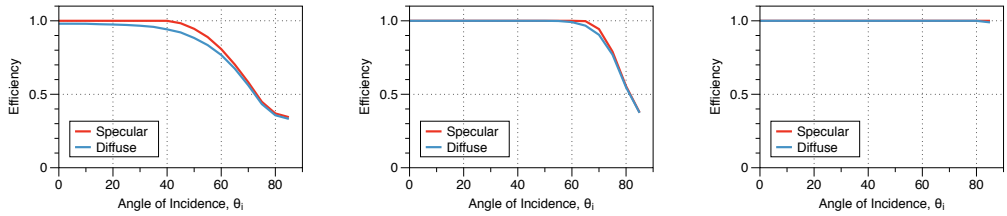

(a) $\delta = 0.098$. 1% error at normal incidence.

(b) $\delta = 0.055$. 1% error from normal to 60°.

(c) $\delta = 0.0105$. 1% error from normal to 85°.

Fig. 9. Detector efficiencies for the detector of Fig. 8. This detector works very well at angles close to normal incidence, but is inefficient towards grazing angles. Note that performance is limited by the diffuse case for normal incidence, as the spot size is overfilling the detectable area.

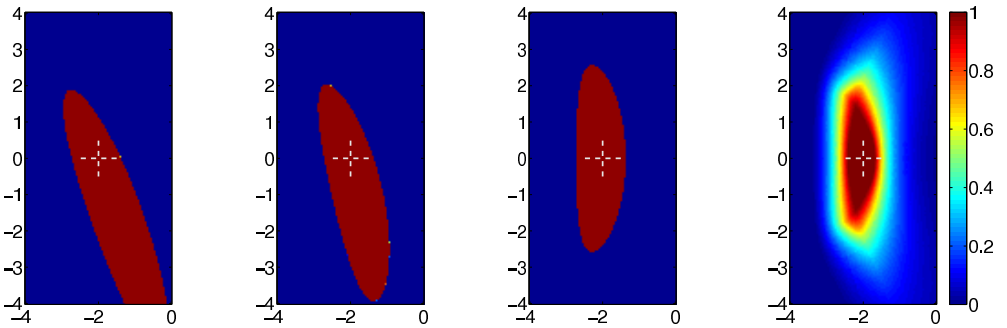

(a) $\theta_i = 85°$

(b) $\theta_i = 45°$

(c) $\theta_i = 0°$

(d) Diffuse Case

Fig. 10. Detectable irradiance map for a elliptical detector with major radius 3.19 units and minor radius 0.798 units (surface area = 8 units-squared). The white cross is the location of the object-space focal point.

a detector half as wide can measure a spot size half as large. From normal incidence to 60°, the new δ is 0.046 with the same error. Of the geometries studied in this section, this detector worked best at grazing angle, measuring a sample with $\delta = 0.0140$ with the same error. This is expected given that the detector is elongated in the same direction as the sample over the course of the measurement. Plots of this detector's efficiency as a function of angle are shown in Fig. 11.

The rectangular detector performs in between the previous two detectors, excelling at neither normal incidence nor grazing angles. Detectable irradiance maps are shown in Fig. 12. For normal incidence, the detector can measure a sample with $\delta = 0.064$ with less than a 1% error. The δ drops slightly for the normal-to-60-degree measurement to 0.057, with the same error. The grazing-angle measurement is significantly lower, dropping to a δ of 0.0130 with the same error. Given the dimensions of the detector, it is not surprising that it functions similarly to the elliptical detector. Plots of this detector's efficiency are shown in Fig. 13.

Changing the eccentricity of the system has a noticeable effect on the performance of the system. Increasing the eccentricity of the mirror decreases the maximum value of δ, which is shown in Fig. 14. For the most part, these effects are linear, which is consistent with the work presented by Brandenburg [1] and Snail [8]. Higher eccentricities have higher magnifications, which implies that the δ would decrease as eccentricity increases. A few of the effects are not

#190358 - $15.00 USD Received 16 May 2013; revised 19 Aug 2013; accepted 22 Aug 2013; published 4 Nov 2013

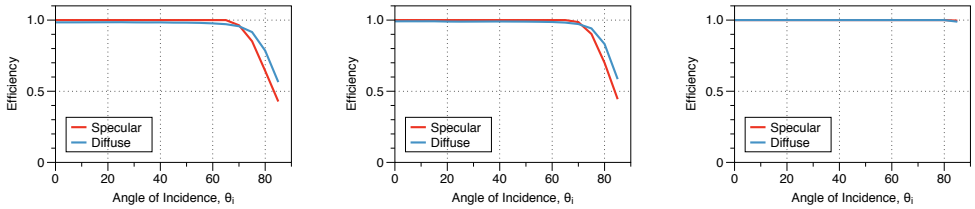

(a) $\delta = 0.050$. 1% error at normal incidence.

(b) $\delta = 0.046$. 1% error from normal to 60°.

(c) $\delta = 0.0140$. 1% error from normal to 85°.

Fig. 11. Detector efficiencies for the detector of Fig. 10. This detector functions better at higher angles of incidence, but has poor performance closer to normal incidence.

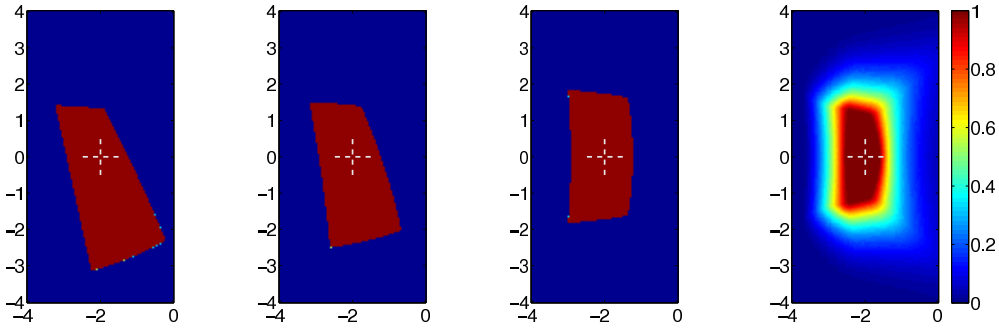

(a) $\theta_i = 85°$

(b) $\theta_i = 45°$

(c) $\theta_i = 0°$

(d) Diffuse Case

Fig. 12. Detectable irradiance map for a rectangular detector with dimensions 4 units long by 2 units wide (surface area = 8 units-squared). The white cross is the location of the object-space focal point.

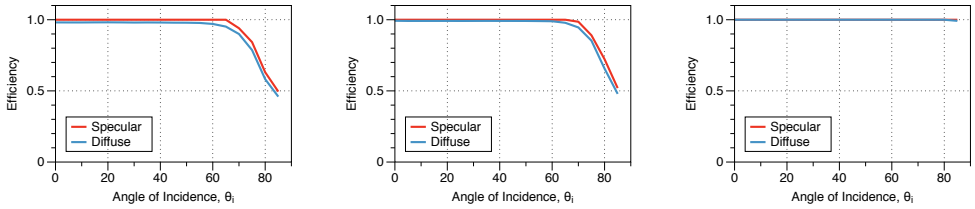

(a) $\delta = 0.064$. 1% error at normal incidence.

(b) $\delta = 0.057$. 1% error from normal to 60°.

(c) $\delta = 0.0130$. 1% error from normal to 85°.

Fig. 13. Detector efficiencies for the detector of Fig. 12. This detector functions slightly better than the elliptical detector at all but the highest angles of incidence.

#190358 - $15.00 USD Received 16 May 2013; revised 19 Aug 2013; accepted 22 Aug 2013; published 4 Nov 2013

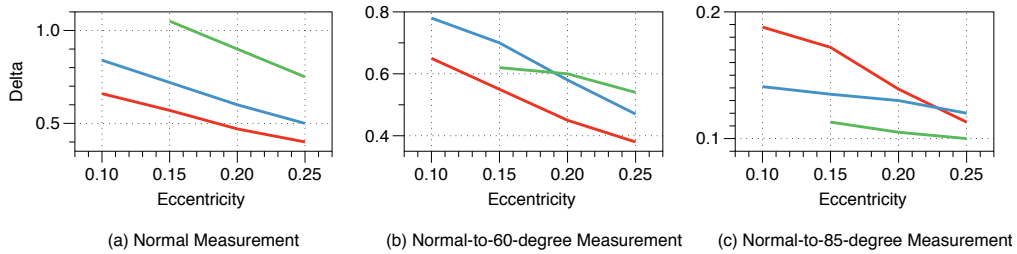

(a) Normal Measurement (b) Normal-to-60-degree Measurement (c) Normal-to-85-degree Measurement

Fig. 14. Maximum δ as a function of mirror eccentricity for the circular detector (in green), the rectangular detector (in blue) and the elliptical detector (in red).

strictly linear in nature, namely, the circular detector used with a mirror with $\varepsilon = 0.15$ and the elliptical detector at higher eccentricities. Nonetheless, they are monotonically decreasing. These effects are primarily due to the mirror distorting the shape of the detectable area more severely at higher eccentricities.

All of these calculations were performed under the assumption that the detector can absorb all of the incident light. The circular detector functions best at angles close to normal incidence, but poorly at high angles of incidence. At very high angles, the rectangular detector performs about as well as the elliptical detector. For the normal-to-60-degree measurements, both the circular and rectangular detectors function similarly. These results are tabulated in Table 1.

Table 1. Maximum spot size for the three detector configurations examined. All spot sizes give less than 1% error over the range of measurements for both specular and diffuse samples. The orange entries represent the largest spot size for the given measurement.

	Normal	Normal to 60°	Normal to 85°
Circle	0.098	0.055	0.0105
Ellipse	0.050	0.046	0.0140
Rectangle	0.064	0.057	0.0130

5. Coupling light into the detector

In practice, the assumption that the detector can absorb all of the incident light is not necessarily true [2,9]. This is made evident by applying the conservation of energy to the detector. The sum of the reflectance, transmission and absorption must be equal to one. Because all surfaces reflect some portion of the light incident on them, they cannot be truly perfect absorbers. In general, this effect can be overlooked, as most systems make measurements with light normally incident upon the detector. Typically, these effects are small and easily removed through calibration routines.

In this case, this cannot be done since reflection is a function of angle. Assuming the transmission is zero,

$$A(\theta,\phi) = 1 - R(\theta,\phi) \tag{7}$$

where A is the detector's absorptance and R is the detector's reflectance. Applying this to Eq.

#190358 - $15.00 USD Received 16 May 2013; revised 19 Aug 2013; accepted 22 Aug 2013; published 4 Nov 2013

(5) gives the total power absorbed by the detector as

$$\begin{aligned}\Phi_d &= \int_{A_o}\int_{\Omega_o} E_0(\mathbf{p}_1) f(\hat{\mathbf{d}}_i, \hat{\mathbf{d}}_1)(\hat{\mathbf{d}}_1 \cdot \hat{\mathbf{z}}) D\left[\mathbf{p}_2(\mathbf{p}_1, \hat{\mathbf{d}}_1)\right] A\left[\hat{\mathbf{d}}_2(\mathbf{p}_1, \hat{\mathbf{d}}_1)\right] \, d\Omega_o \, dA_o \\ &= \int_{A_o} E_0(\mathbf{p}_1) E_A(\mathbf{p}_1, \hat{\mathbf{d}}_1) \, dA_o \end{aligned} \tag{8}$$

where

$$E_A(\mathbf{p}_1, \hat{\mathbf{d}}_1) \equiv \int_{\Omega_o} f(\hat{\mathbf{d}}_i, \hat{\mathbf{d}}_1)(\hat{\mathbf{d}}_1 \cdot \hat{\mathbf{z}}) D\left[\mathbf{p}_2(\mathbf{p}_1, \hat{\mathbf{d}}_1)\right] A\left[\hat{\mathbf{d}}_2(\mathbf{p}_1, \hat{\mathbf{d}}_1)\right] \, d\Omega_o \tag{9}$$

This detected irradiance map, E_A, is equivalent to the detected irradiance map detailed in Section 4, but now includes the effects of the detector's absorptance.

In Section 4, two different scatter patterns were examined: the diffuse case and the specular case. With the specular case, the angle of the incident light is known. From this, with a good detector model, the absorption term the detector can be calculated, and the data can be compensated accordingly. For the diffuse case, the absorption term must be integrated over the entire 2π steradians of the detector, which gives an effective absorption coefficient for the sample. In general, this will lead to a different compensation than for the specular case. The data could again be properly compensated, and used to arrive at the proper measurement.

In practice, neither of these compensations are acceptable. Both of them require knowing the scatter pattern of the sample before the measurement, making the measurement moot. In addition, no sample is perfectly specular or perfectly diffuse. Any real sample has attributes of both, meaning that any proposed compensation would have to be calculated specifically for that sample. Again, this would be a very poor way to make measurements.

This effect is limited to reflectometers which make measurements in this fashion. For example, the Surface Optics Corp.'s instrument, the SOC-100, makes HDR (Hemispherical Directional Reflectance) measurements by illuminating the sample equally from all directions, then making the measurement from a single angle of reflectance [10]. Because of this, light always enters the detector at normal incidence, negating this effect. Instruments such as Northrop Grumman Corp.'s instrument, the Infrared Grazing Angle Reflectometer (IGAR), absorb light more indiscriminately, and these effects must be considered during the design of the instrument [11, 12].

There are two ways to address this effect. One is to simply limit the range of usable angles [13]. For example, assuming that the detector has a Fresnel reflectance (with $n_{\text{air}} = 1$ and $n_{\text{detector}} = 2$), the reflectance changes 5% over the range from normal incidence to 56°. As seen in Eq. (7), the absorption depends on the reflectance of the detector. Due to the conservation of energy, a surface which reflects light uniformly over a wide range of angles will absorb light uniformly over a wide range of angles. This would allow the detector to make more accurate measurements over a wider range of angles.

In the following simulations, the model used for the absorber is simply Eq. (7), using Fresnel reflectance with $n_{\text{incident}} = 1$ and $n_{\text{detector}} = 2$. In practice, this reflectance function for the detector would be replaced with either a spectral DHR measurement of the detector surface, or the absorption with a measurement of detector absorption as a function of angle. This particular model was chosen as it is easy to model, and demonstrates the relevant characteristics of this system. Note that the same mirror described in Section 2 ($\varepsilon = 0.2$) is used.

The absorption-based detected irradiance maps for a circular detector are shown in Fig. 15. Taking absorption into account, the first thing to notice is that the minimum error of the system increases dramatically, even with proper calibration. The minimum error for a point source is 3.2%, up from 1% from the ideal case shown in Fig. 8. For a circular detector at normal incidence, the δ drops from 0.098 to 0.080, with the maximum error increasing to 3.5%. This

#190358 - $15.00 USD Received 16 May 2013; revised 19 Aug 2013; accepted 22 Aug 2013; published 4 Nov 2013

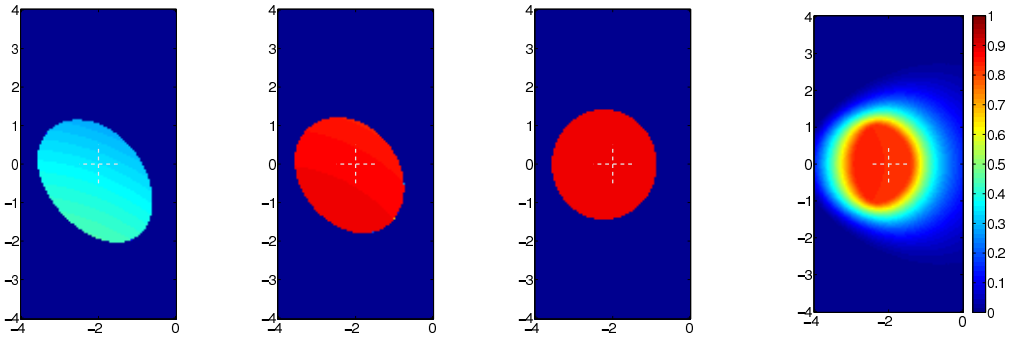

(a) $\theta_i = 85°$ (b) $\theta_i = 45°$ (c) $\theta_i = 0°$ (d) Diffuse Case

Fig. 15. Detectable irradiance maps for a circular detector with radius 1.618 units (surface area = 8 units-squared), taking absorption into account. The white cross is the location of the object-space focal point.

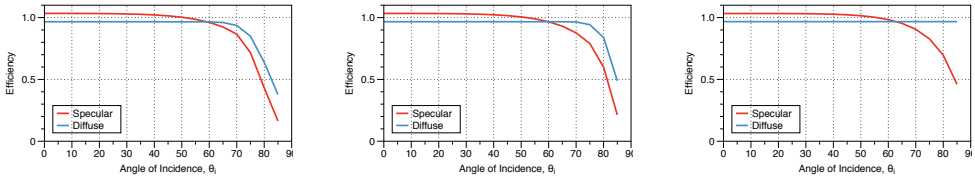

(a) $\delta = 0.045$. 3.5% error at normal incidence.

(b) $\delta = 0.030$ 3.5% error from normal to 60°.

(c) $\delta = 0$. Unusable for measurements.

Fig. 16. Detector efficiencies for the detector of Fig. 15. Note that the minimum error in the measurement is significantly higher than in the perfect absorber case (3.2% here, as opposed to the 1% error presented in Fig. 9). The limiting case cannot make measurements past 60°.

greater baseline error is due to the error introduced by the absorption term into the diffuse case, which will be examined in the following paragraph. For the normal-to-60-degree measurement, the δ decreases to 0.029, with a similar error. Due to the Fresnel reflectance, this detector is incapable of making measurements at grazing angles. Detector efficiencies as a function of angle are shown in Fig. 16.

The fact that the minimum spot size for an absorption-based model is smaller than the minimum spot size for the perfect absorption case is due to how the hemi-ellipsoidal mirror reflects light to the second focal point. Light emitted from points towards the center of the mirror tend to have their angle of incidence changed less than points further away from the center. This means that the rays that are emitted from points closer to the center of the mirror at close-to-normal incidence strike the detector closer to normal incidence. Because the Fresnel reflection is lower at normal incidence, the rays are more accurately detected.

Both the rectangular detector and elliptical detector function very similarly to the circular detector. The elliptical detector's performance was significantly worse than the ideal case, and will not be examined here. For the rectangular detector, detectable irradiance maps are shown in Fig. 17. The minimum error for all cases is slightly greater than the circular case, increasing 1% in Fig. 12 to 3.4%. At normal incidence, δ is 0.043, with a maximum error of 3.5%. This is a decrease from the δ of 0.064 in the perfectly absorbing case. Of note, this spot size was also useable for the normal-to-60-degree measurement with the same error. Again, even in the

#190358 - $15.00 USD Received 16 May 2013; revised 19 Aug 2013; accepted 22 Aug 2013; published 4 Nov 2013

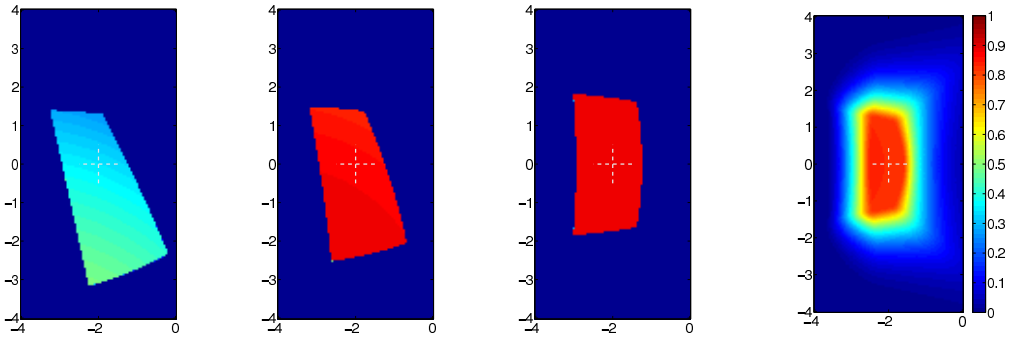

(a) $\theta_i = 85°$ (b) $\theta_i = 45°$ (c) $\theta_i = 0°$ (d) Diffuse Case

Fig. 17. Detectable irradiance maps for a rectangular detector with 4 units long and 2 units wide, (Surface area = 8 units-squared) taking absorption into account. The white cross is the location of the object-space focal point.

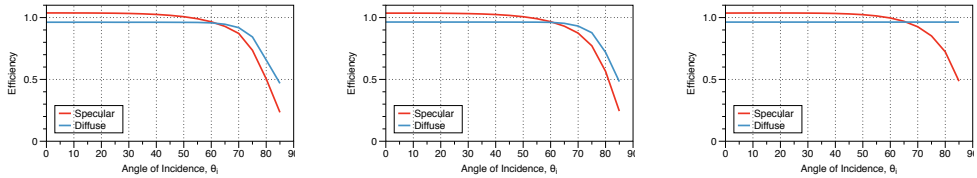

(a) $\delta = 0.55$. 3.5% error at normal incidence.

(b) $\delta = 0.049$. 3.5% error from normal to 60°.

(c) $\delta = 0$. Unusable for measurements.

Fig. 18. Detector efficiencies for the detector of Fig. 17. This detector has a larger usable area in sample space than the circular detector, but still functions poorly.

limiting case, the system cannot accurately measure grazing angles due to the absorption curve of the detector. Detector efficiencies as a function of angle are shown in Fig. 18.

The final detector configuration considered here is the multifaceted, parallel-piped-shaped detector (as seen in instruments such as the IGAR) [11, 12]. This detector is five-sided, which is meant to minimize reflectance effects by coupling light into the detector at closer-to-normal incidence over the range of measurements. In practice, this detector functions best of the detectors examined here. The associated detectable irradiance maps are shown in Fig. 19. At normal incidence, this detector performs better than the circular detector. With a δ of 0.072, the associated error is 1%. For the normal-to-60-degree measurement, the detector can measure a sample with $\delta = 0.025$ with an error of 3.5%. At grazing angles, the detector can still measure samples with $\delta = 0.0110$ with a maximum error of 3.5%. Detector efficiencies as a function of angle are shown in Fig. 20.

The effects of mirror eccentricity on a system with a multifaceted, this this case parallel-piped, detector are much different than the detectors examined in Section 4, and is shown in 21. The performance of the mirror is again monotonically decreasing for the normal-to-60-degree measurement and the normal-to-85-degree measurement. They follow the same trends as shown in Fig. 14, only much less strictly. Still, lowering the eccentricity increases the maximum value of δ.

This is not the case for the normal measurement. Here, an eccentricity of 0.2 gives peak performance, which is nearly 10% higher than the case of $\varepsilon = 0.1$. This is due to a crossover point in efficiency between the specular measurement and the diffuse measurement. At lower

#190358 - $15.00 USD Received 16 May 2013; revised 19 Aug 2013; accepted 22 Aug 2013; published 4 Nov 2013

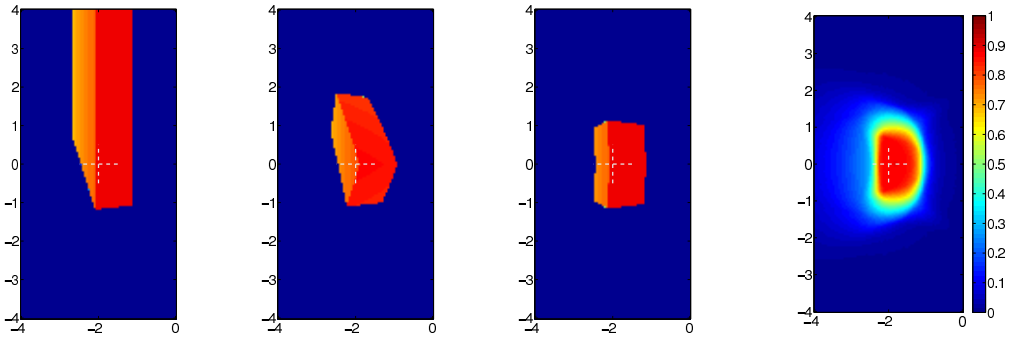

(a) $\theta_i = 85°$ (b) $\theta_i = 45°$ (c) $\theta_i = 0°$ (d) Diffuse Case

Fig. 19. Detectable irradiance maps for a parallel-piped detector with dimensions 1 unit tall by 1 unit wide by 2 units long (surface area = 8 units-squared), taking absorption into account. The white cross is the location of the object-space focal point.

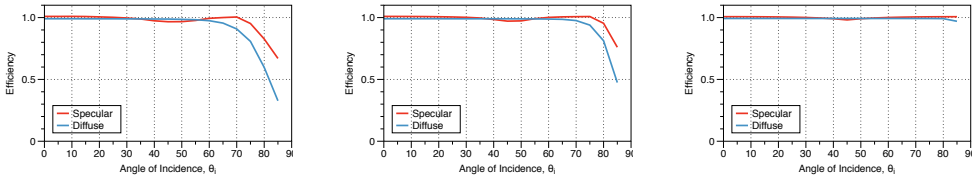

(a) $\delta = 0.040$. 1% error at normal incidence. (b) $\delta = 0.027$. 1% error from normal to 60°. (c) $\delta = 0.0080$. 1% error from normal to 85°.

Fig. 20. Detector efficiencies for the detector of Fig. 19. This detector has much smaller errors than the flat detectors examined, and can be used to make accurate grazing-angle measurements.

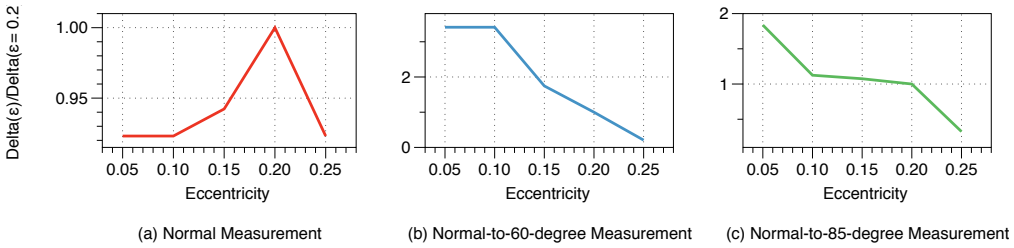

Fig. 21. Maximum δ as a function of mirror eccentricity for the case of a parallel-piped detector. Omitting the normal incidence case, the overall trends are similar, but not the same, as with the perfectly absorbing detector.

eccentricities, the specular measurement limits the value of δ, while the diffuse case is the limiting factor at higher eccentricities. While neither measurement is ideal at this particular eccentricity, δ is optimal here.

These results are tabulated in Table 2. Both the circular and the rectangular detectors have significantly higher errors than their perfectly absorbing counterparts discussed earlier. Even with the higher error, the spot size decreases significantly. Interestingly, the rectangular detector works better than the circular detector at normal incidence, the opposite of what was found in Section 4. The circular detector performs better than the rectangular detector at higher

#190358 - $15.00 USD Received 16 May 2013; revised 19 Aug 2013; accepted 22 Aug 2013; published 4 Nov 2013

angles of incidence. The five-sided detector functions much better than the flat detectors, maintaining an error comparable to the perfectly absorbing cases of the flat detectors. While the spot sizes are significantly smaller, this detector can be used to make highly accurate reflectance measurements.

Table 2. Maximum spot size for the three detector configurations examined. The green cells indicate the measurement has $< 1\%$ error. The yellow cells indicate $< 3.5\%$ error, and the red cells indicate that the error is too high to make a measurement.

	Normal	Normal to 60°	Normal to 85°
Circle	0.045	0.060	-
Rectangle	0.055	0.049	-
Five Sided Detector	0.040	0.027	0.0080

6. Conclusion

Previous attempts to model hemi-ellipsoidal mirrors have relied on simplified geometric models which prevented them from being used in radiometrically accurate models. By defining both the object point and direction of the emitted rays, our formulation can be used to properly model the transfer of energy from object space into image space. The image distortions of both diffuse and specular samples were examined. It is important to note that the blur spot of the object point is dependent on the location of the object. This analysis applied to systems making DHR measurements shows that a circular detector is optimal for DHR measurements close to normal incidence, while a rectangular-shaped detector properly measures reflectance over a wider range of angles. Mirror eccentricity plays a role in system performance in that mirrors with lower eccentricities perform better.

Finally, the DHR measuring system was simulated using a detector with imperfect absorption, since real flat detectors cannot properly measure over 2π steradians. This simulation, based on Fresnel reflectance, showed that a system using a flat detector can only properly measure reflectance over a range from normal to 45 degrees. A more complex detection system, such as a five-sided parallel-piped detector, can make accurate measurements at normal incidence through grazing angles. Adjusting the eccentricity while accounting for detector absorption creates similar trends as for the case of the ideal detector.

Hemi-ellipsoidal mirrors can be used to accurately measure DHR over a wide range of angles, provided that a wide range of system characteristics are considered during the design of the instrument. The two most important design considerations are the deformation of the area of detection as the angle of incidence changes, and the ability of the detector to properly measure the incident light. Neither attribute is difficult to address during system design, but must be addressed to ensure measurement accuracy.

#190358 - $15.00 USD Received 16 May 2013; revised 19 Aug 2013; accepted 22 Aug 2013; published 4 Nov 2013